

1

2 Modular strategies for spatial mapping of 3 multi-modal mouse brain data

4 Nicholas J. Tustison¹, Min Chen², Fae N. Kronman³, Jeffrey T. Duda², Clare Gamlin⁴, Mia
5 G. Tustison, Michael Kunst⁴, Rachel Dalley⁴, Staci Sorenson⁴, Quanxin Wang⁴, Lydia Ng⁴,
6 Yongsoo Kim³, and James C. Gee²

7 ¹Department of Radiology and Medical Imaging, University of Virginia, Charlottesville, VA

8 ²Department of Radiology, University of Pennsylvania, Philadelphia, PA

9 ³Department of Neural and Behavioral Sciences, Penn State University, Hershey, PA

10 ⁴Allen Institute for Brain Science, Seattle, WA

11

12 Corresponding authors:

13

14 Nicholas J. Tustison, DSc

15 Department of Radiology and Medical Imaging

16 University of Virginia

17 ntustison@virginia.edu

18

19 James C. Gee, PhD

20 Department of Radiology

21 University of Pennsylvania

22 gee@upenn.edu

²³ **Abstract**

²⁴ Large-scale efforts by the BRAIN Initiative Cell Census Network (BICCN) are generating
²⁵ a comprehensive reference atlas of cell types in the mouse brain. A key challenge in this
²⁶ effort is mapping diverse datasets, acquired with varied imaging, tissue processing, and
²⁷ profiling methods, into shared coordinate frameworks. Here, we present modular mapping
²⁸ pipelines developed using the Advanced Normalization Tools Ecosystem (ANTsX) to align
²⁹ MERFISH spatial transcriptomics and high-resolution fMOST morphology data to the Allen
³⁰ Common Coordinate Framework (CCFv3), and developmental MRI and LSFM data to the
³¹ Developmental CCF (DevCCF). Simultaneously, we introduce two novel methods: 1) a
³² velocity field-based approach for continuous interpolation across developmental timepoints,
³³ and 2) a deep learning framework for automated brain parcellation using minimally annotated
³⁴ and publicly available data. All workflows are open-source and reproducible. We also provide
³⁵ general guidance for selecting appropriate strategies across modalities, enabling researchers
³⁶ to adapt these tools to new data.

³⁷ 1 Introduction

³⁸ Over the past decade, there have been significant advancements in mesoscopic single-cell
³⁹ analysis of the mouse brain. It is now possible to track single neurons¹, observe whole-
⁴⁰ brain developmental changes at cellular resolution², associate brain regions with genetic
⁴¹ composition³, and locally characterize neural connectivity⁴. These scientific achievements have
⁴² been propelled by high-resolution profiling and imaging techniques that enable submicron,
⁴³ multimodal, three-dimensional characterizations of whole mouse brains. Among these are
⁴⁴ micro-optical sectioning tomography^{5,6}, tissue clearing methods^{1,7}, spatial transcriptomics^{8,9},
⁴⁵ and single-cell genomic profiling¹⁰, each offering expanded specificity and resolution for
⁴⁶ cell-level brain analysis.

⁴⁷ Recent efforts by the NIH BRAIN Initiative have mobilized large-scale international col-
⁴⁸ laborations to create a comprehensive reference database of mouse brain structure and
⁴⁹ function. The BRAIN Initiative Cell Census Network has aggregated over 40 multimodal
⁵⁰ datasets from more than 30 research groups¹¹, many of which are registered to standardized
⁵¹ anatomical coordinate systems to support integrated analysis. Among the most widely used
⁵² of these frameworks is the Allen Mouse Brain Common Coordinate Framework (CCFv3)¹².
⁵³ Other CCFs include modality-specific references^{13–15} and developmental atlases^{16,17} that track
⁵⁴ structural change across time.

⁵⁵ 1.1 Mouse brain mapping challenges

⁵⁶ Robust mapping of cell type data into CCFs is essential for integrative analysis of morphology,
⁵⁷ connectivity, and molecular identity. However, each modality poses unique challenges. For
⁵⁸ example, differences in tissue processing, imaging protocols, and anatomical completeness
⁵⁹ often introduce artifacts such as distortion, tearing, holes, and signal dropout^{18–23}. Intensity
⁶⁰ differences and partial representations of anatomy can further complicate alignment. Given
⁶¹ this diversity specialized strategies are often needed to address the unique, modality-specific
⁶² challenges.

⁶³ Existing mapping solutions fall into three broad categories. The first includes integrated

64 processing platforms that provide users with mapped datasets (e.g., Allen Brain Cell Atlas²⁴,
65 Brain Architecture Portal²⁵, OpenBrainMap²⁶, and Image and Multi-Morphology Pipeline²⁷).
66 These offer convenience and high-quality curated data, but limited generalizability and
67 customization. The second category involves highly specialized pipelines tailored to specific
68 modalities such as histology^{28–30}, magnetic resonance imaging (MRI)^{31–33}, microCT^{34,35}, light
69 sheet fluorescence microscopy (LSFM)^{36,37}, fluorescence micro-optical sectioning tomography
70 (fMOST)^{15,38}, and spatial transcriptomics, including multiplexed error-robust fluorescence in
71 situ hybridization (MERFISH)^{39–41}. While effective, these solutions often require extensive
72 engineering effort to adapt to new datasets or modalities. Finally, general-purpose toolkits
73 such as elastix⁴², Slicer3D⁴³, and the Advanced Normalization Tools Ecosystem (ANTsX)⁴⁴
74 have all been applied to mouse brain mapping scenarios (e.g., SlicerMEMOS⁴⁵). These
75 toolkits support modular workflows that can be flexibly composed from reusable components,
76 offering a powerful alternative to rigid, modality-specific solutions. However, their use often
77 requires familiarity with pipeline modules, parameter tuning, and tool-specific conventions
78 which can limit adoption.

79 Building on this third category, we describe a set of modular, ANTsX-based pipelines
80 specifically tailored for mapping diverse mouse brain data into standardized anatomical
81 frameworks. These include two new pipelines: a velocity field-based interpolation model that
82 potentially enables biologically plausible transformations across developmental timepoints, and
83 a template-based deep learning pipeline for brain extraction and parcellation requiring minimal
84 annotated data. In addition, we include two modular pipelines for aligning multiplexed
85 error-robust fluorescence in situ hybridization (MERFISH) and fMOST datasets to the
86 Allen CCFv3. These workflows were adapted and tailored using ANTsX tools to support
87 collaborative efforts within the BICCN and are now made openly available in a reproducible
88 format. To facilitate broader adoption, we also provide general guidance for customizing
89 these strategies across imaging modalities and data types. We first introduce key components
90 of the ANTsX toolkit, which provide a basis for all of the mapping workflows described here,
91 and then detail the specific contributions made in each pipeline.

92 1.2 The Advanced Normalization Tools Ecosystem (ANTsX)

93 The Advanced Normalization Tools Ecosystem (ANTsX) has been used in a number of
94 applications for mapping mouse brain data as part of core processing steps in various
95 workflows^{30,46–49}, particularly its pairwise, intensity-based image registration capabilities⁵⁰
96 and bias field correction⁵¹. Historically, ANTsX development is based on foundational
97 approaches to image mapping^{52–54}, especially in the human brain, with key contributions such
98 as the Symmetric Normalization (SyN) algorithm⁵⁰. It has been independently evaluated in
99 diverse imaging domains including multi-site brain MRI⁵⁵, pulmonary CT⁵⁶, and multi-modal
100 brain tumor registration⁵⁷.

101 Beyond registration, ANTsX provides functionality for template generation⁵⁸, intensity-based
102 segmentation⁵⁹, preprocessing^{51,60}, and deep learning⁴⁴. It has demonstrated strong perfor-
103 mance in consensus labeling⁶¹, brain tumor segmentation⁶², and cardiac motion estimation⁶³.
104 Built on the Insight Toolkit (ITK)⁶⁴, ANTsX benefits from open-source contributions while
105 supporting continued algorithm evaluation and innovation. In the context of mouse brain
106 data, ANTsX provides a robust platform for developing modular pipelines to map diverse
107 imaging modalities into CCFs. This paper highlights its use across distinct BICCN projects
108 such as spatial transcriptomic data from MERFISH, structural data from fMOST, and
109 multimodal developmental data from LSFM and MRI. We describe both shared infrastructure
110 and targeted strategies adapted to the specific challenges of each modality.

111 1.3 Novel ANTsX-based open-source contributions

112 We introduce two novel contributions to ANTsX developed as part of collabortive efforts in
113 creating the Developmental Common Coordinate Framework (DevCCF)¹⁶. First, we present
114 an open-source velocity field-based interpolation framework for continuous mapping across the
115 sampled embryonic and postnatal stages of the DevCCF atlas¹⁶. This functionality enables
116 biologically plausible interpolation between timepoints via a time-parameterized diffeomorphic
117 velocity model⁶⁵, inspired by previous work⁶⁶. Second, we present a deep learning pipeline for
118 structural parcellation of the mouse brain from multimodal MRI data. This includes two novel

¹¹⁹ components: 1) a template-derived brain extraction model using augmented data from two
¹²⁰ ANTsX-derived template datasets^{67,68}, and 2) a template-derived parcellation model trained
¹²¹ on DevCCF P56 labelings mapped from the AllenCCFv3. This pipeline demonstrates how
¹²² ANTsX tools and public resources can be leveraged to build robust anatomical segmentation
¹²³ pipelines with minimal annotated data. We independently evaluate this framework using a
¹²⁴ longitudinal external dataset⁶⁹, demonstrating generalizability across specimens and imaging
¹²⁵ protocols. All components are openly available through the R and Python ANTsX packages,
¹²⁶ with general-purpose functionality documented in a reproducible, cross-platform tutorial
¹²⁷ (<https://tinyurl.com/antsxtutorial>). Code specific to this manuscript, including scripts to
¹²⁸ reproduce the novel contributions and all associated evaluations, is provided in a dedicated
¹²⁹ repository (<https://github.com/ntustison/ANTsXMouseBrainMapping>). Additional tools for
¹³⁰ mapping spatial transcriptomic (MERFISH) and structural (fMOST) data to the AllenCCFv3
¹³¹ are separately available at (<https://github.com/dontminchenit/CCFAlignmentToolkit>).

132 **2 Results**

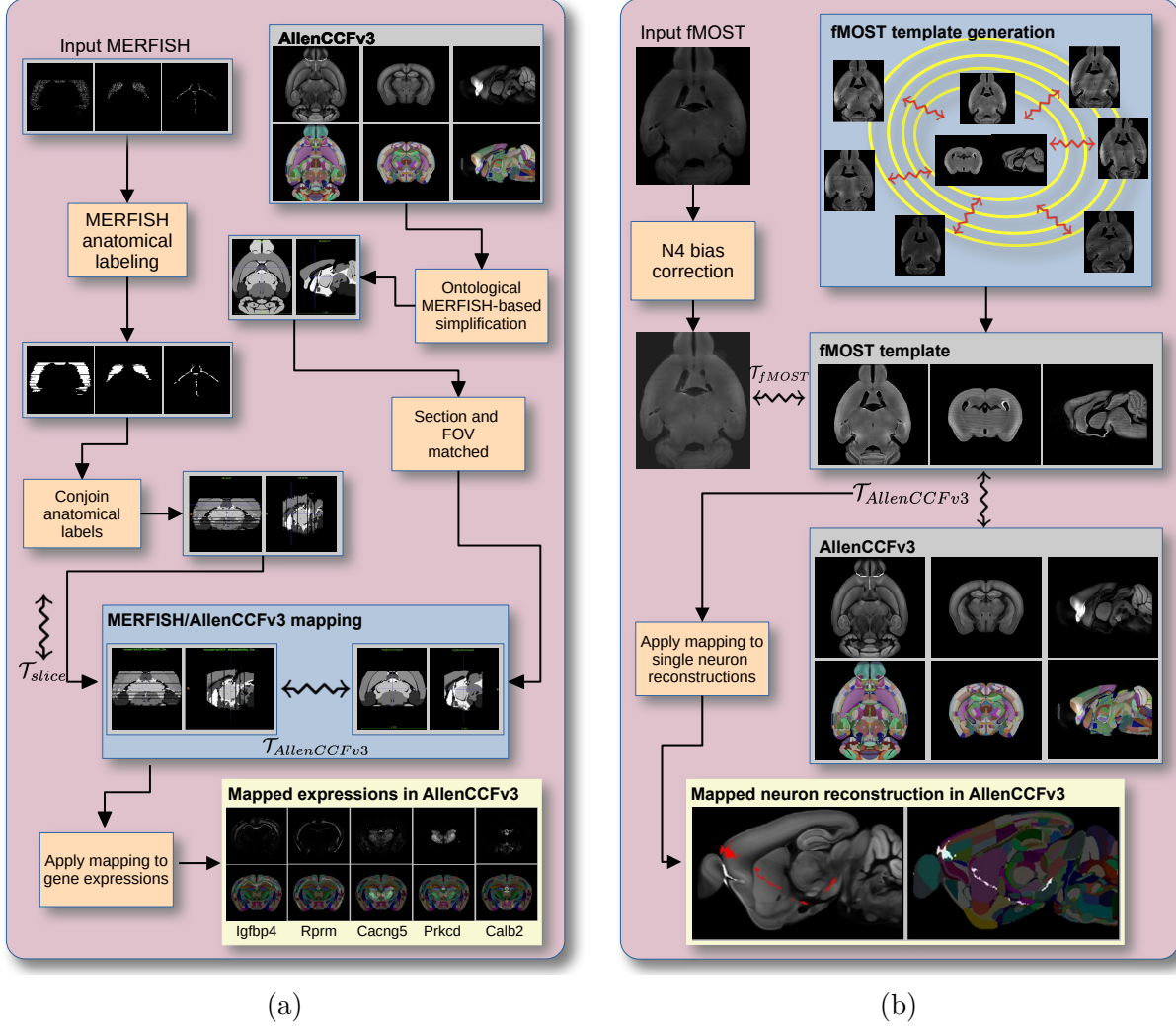


Figure 1: Diagram of the two ANTsX-based pipelines for mapping (a) MERFISH and (b)fMOST data into the space of AllenCCFv3. Each generates the requisite transforms, \mathcal{T} , to map individual images to the CCF.

133 **2.1 AllenCCFv3 brain image mapping**

134 **2.1.1 Mapping multiplexed error-robust fluorescence *in situ* hybridization
135 (MERFISH) data**

136 **Overview.** We developed an ANTsX-based pipeline to map spatial transcriptomic MERFISH
137 data into the AllenCCFv3 (Figure 1(a)). This approach was used in recent efforts to create a

138 high-resolution transcriptomic atlas of the mouse brain⁴⁹. The pipeline maps spatial gene
139 expression patterns from MERFISH onto anatomical labels in the AllenCCFv3. It includes
140 MERFISH-specific preprocessing steps such as section reconstruction, label generation from
141 spatial transcriptomic maps, and anatomical correspondence mapping. Alignment proceeds
142 in two stages: 1) 3D affine registration and section matching of the AllenCCFv3 to the
143 MERFISH data, and 2) linear + deformable 2D section-wise alignment between matched
144 MERFISH and atlas slices. These transformations are concatenated to produce a complete
145 mapping from each MERFISH data to AllenCCFv3.

146 **Data.** MERFISH imaging was performed on cryosectioned brains from C57BL/6 mice using
147 previously described protocols⁴⁹. Brains were placed into an optimal cutting temperature
148 (OCT) compound (Sakura FineTek 4583) stored at -80°. The fresh frozen brain was sectioned
149 at 10 μm on Leica 3050 S cryostats at intervals of 200 μm to evenly cover the brain. A set
150 of 500 genes was selected to distinguish \sim 5200 transcriptomic clusters. Raw MERSCOPE
151 data were decoded using Vizgen software (v231). Cell segmentation was performed using
152 Cellpose^{70,71} based on DAPI and PolyT stains which was propagated to adjacent slices across
153 z-planes. Each MERFISH cell was assigned a transcriptomic identity by mapping to a
154 scRNA-seq reference taxonomy.

155 **Evaluation.** Alignment quality was evaluated iteratively by an expert anatomist, guided
156 by expected gene-marker correspondences to AllenCCFv3 regions. As previously reported⁴⁹,
157 of the 554 terminal gray matter regions in the AllenCCFv3, only seven small subregions
158 were not represented in the MERFISH dataset: frontal pole layer 1 (FRP1), FRP2/3, FRP5;
159 accessory olfactory bulb glomerular (AOBgl), granular (AOBgr), and mitral (AOBmi) layers;
160 and the accessory supraoptic group (ASO).

161 2.1.2 Mapping fluorescence micro-optical sectioning tomography (fMOST) data

162 **Overview.** We also constructed a pipeline for mapping fMOST images to the AllenCCFv3
163 using ANTsX (Figure 1(b)). The approach leverages a modality-specific average fMOST
164 atlas as an intermediate target, adapted from previous work in human and mouse brain
165 mapping^{12,15,16,58,72–75}. The atlas was constructed from 30 fMOST images selected to capture

¹⁶⁶ representative variability in anatomical shape and image intensity across the population.
¹⁶⁷ Preprocessing includes cubic B-spline downsampling to match the $25\text{ }\mu\text{m}$ isotropic AllenCCFv3
¹⁶⁸ resolution, stripe artifact suppression using a 3D notch filter implemented with SciPy's
¹⁶⁹ frequency-domain filtering tools, and N4 bias field correction⁵¹. A one-time, annotation-
¹⁷⁰ driven alignment registers the fMOST atlas to AllenCCFv3 using landmark-based registration
¹⁷¹ of key structures. This canonical mapping is then reused. New fMOST specimens are first
¹⁷² aligned to the fMOST atlas using standard intensity-based registration, and the concatenated
¹⁷³ transforms yield full spatial normalization to the AllenCCFv3. This same mapping can be
¹⁷⁴ applied to neuron reconstructions to facilitate population-level analysis of morphology and
¹⁷⁵ spatial distribution.

¹⁷⁶ **Data.** fMOST imaging was performed on 55 mouse brains with sparse transgenic labeling of
¹⁷⁷ neuron populations^{76,77} using the high-throughput fMOST platform^{78,79}. Voxel resolution was
¹⁷⁸ $0.35 \times 0.35 \times 1.0\text{ }\mu\text{m}^3$. Two imaging channels were acquired: GFP-labeled neuron morphology
¹⁷⁹ (green), and propidium iodide counterstaining for cytoarchitecture (red). Alignment was
¹⁸⁰ performed using the red channel for its greater contrast, though multi-channel mapping is
¹⁸¹ also supported.

¹⁸² **Evaluation.** The canonical mapping from the fMOST atlas to AllenCCFv3 was evaluated
¹⁸³ using both quantitative and qualitative approaches. Dice similarity coefficients were computed
¹⁸⁴ between corresponding anatomical labels in the fMOST atlas and AllenCCFv3 following
¹⁸⁵ registration. These labels were manually annotated or adapted from existing atlas segmen-
¹⁸⁶ tations. Representative Dice scores included: whole brain (0.99), caudate putamen (0.97),
¹⁸⁷ fimbria (0.91), posterior choroid plexus (0.93), anterior choroid plexus (0.96), optic chiasm
¹⁸⁸ (0.77), and habenular commissure (0.63). In addition to these quantitative assessments,
¹⁸⁹ each registered fMOST specimen was evaluated qualitatively. An expert anatomist reviewed
¹⁹⁰ alignment accuracy and confirmed structural correspondence. Neuron reconstructions from
¹⁹¹ individual brains were also transformed into AllenCCFv3 space, and their trajectories were
¹⁹² visually inspected to confirm anatomical plausibility and preservation of known projection
¹⁹³ patterns.

¹⁹⁴ 2.2 Continuously mapping the DevCCF developmental trajectory

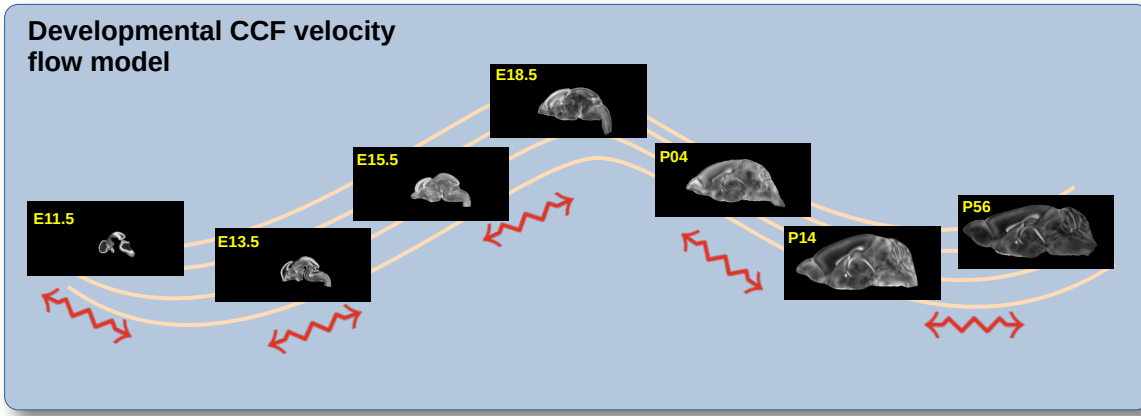


Figure 2: The spatial transformation between any two time points within the continuous DevCCF longitudinal developmental trajectory is available through the use of ANTsX functionality for generating a velocity flow model.

¹⁹⁵ The DevCCF is an openly accessible resource for the mouse brain research community⁸⁰,
¹⁹⁶ comprising symmetric, multi-modal MRI and LSFM templates generated using the ANTsX
¹⁹⁷ framework⁵⁸. It spans key stages of mouse brain development (E11.5, E13.5, E15.5, E18.5,
¹⁹⁸ P4, P14, and P56) and includes structural labels defined by a developmental ontology. The
¹⁹⁹ DevCCF was constructed in coordination with the AllenCCFv3 to facilitate integration across
²⁰⁰ atlases and data types.

²⁰¹ Although this collection provides broad developmental coverage, its discrete sampling
²⁰² limits the ability to model continuous transformations across time. To address this,
²⁰³ we developed a velocity flow-based modeling approach that enables anatomically plau-
²⁰⁴ sible, diffeomorphic transformations between any two continuous time points within
²⁰⁵ the DevCCF range. This functionality is implemented in both ANTsR and ANTsPy
²⁰⁶ (`ants.fit_time_varying_transform_to_point_sets(...)`) and integrates seamlessly with
²⁰⁷ existing ANTsX workflows. The velocity field is encoded as a 4D ITK image where each
²⁰⁸ voxel stores the x,y,z components of motion at a given time point.

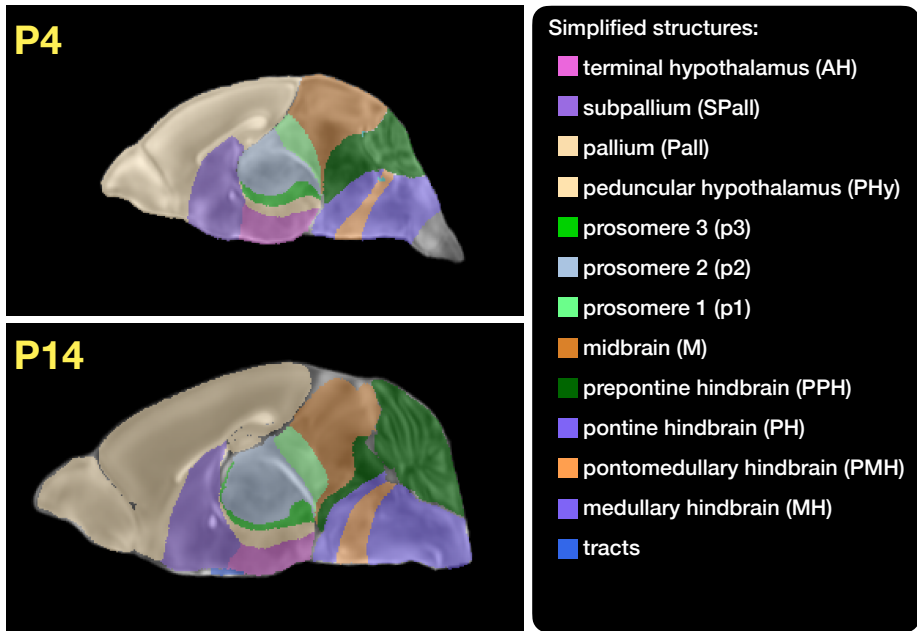


Figure 3: Annotated regions representing common labels across developmental stages, shown for both P4 and P14.

2.2.1 Data

Each DevCCF template includes over 2,500 labeled anatomical regions, with spatial resolutions ranging from 31.5 to 50 μ m. For the velocity flow modeling task, we identified a common set of 26 bilateral regions (13 per hemisphere) that were consistently labeled across all timepoints. These regions span major developmental domains including the pallium, subpallium, midbrain, prosomeres, hypothalamus, hindbrain subregions, and key white matter tracts (Figure 3).

Prior to velocity field optimization, all templates were rigidly aligned to the DevCCF P56 template using the centroids of these common label sets. Pairwise correspondence between adjacent timepoints was then computed using ANTsX's multi-metric registration via `ants.registration(...)`. Instead of performing intensity-based multi-label registration directly, we constructed 24 binary label masks per atlas pair (one per structure) and optimized alignment using the mean squares similarity metric with the SyN transform⁵⁰.

To generate the point sets for velocity field optimization, we sampled both boundary (contour) and interior (region) points from the P56 labels and propagated them to each developmental stage using the learned pairwise transforms. Contours were sampled at 10% of available points

²²⁴ and regions at 1%, yielding 173,303 total points per atlas ($N_{contour} = 98,151$; $N_{region} = 75,152$).
²²⁵ Boundary points were assigned double weight during optimization to emphasize anatomical
²²⁶ boundary correspondence.

²²⁷ **2.2.2 Velocity field optimization**

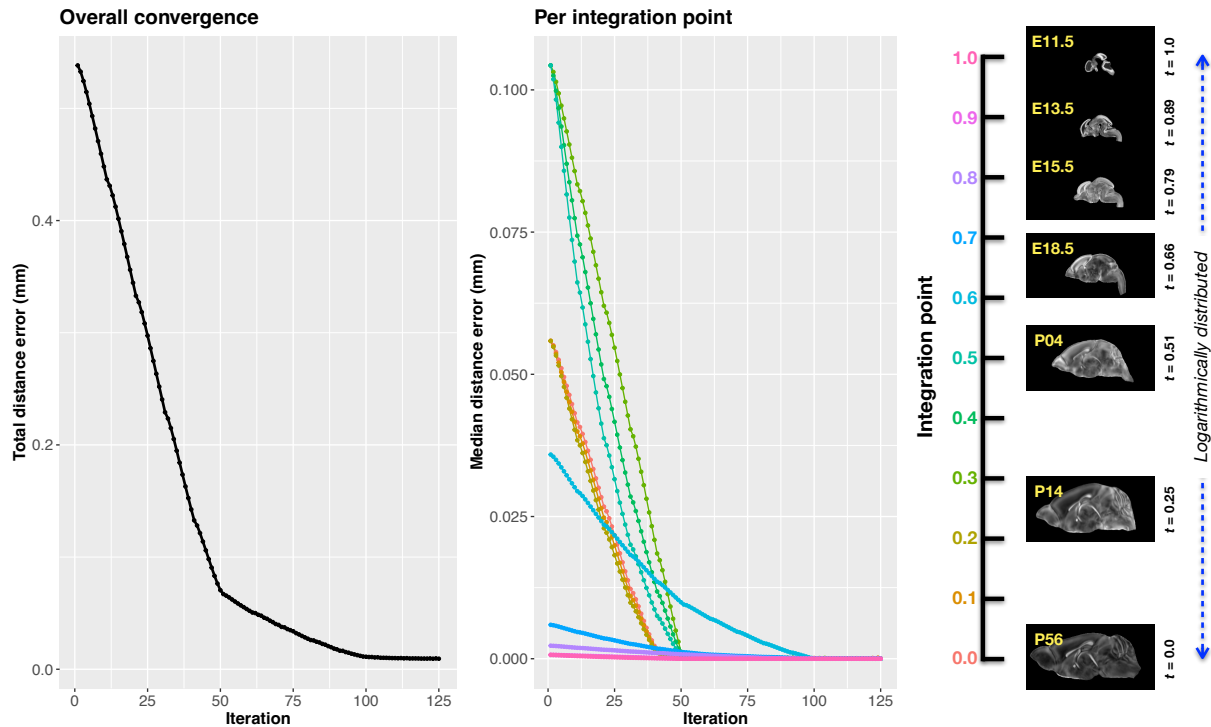


Figure 4: Convergence of velocity field optimization across the DevCCF developmental trajectory. Integration points (color-coded) are distributed along the log-scaled time axis.

²²⁸ The velocity field was optimized using the seven corresponding point sets and their associated
²²⁹ weights. The field geometry was defined at [256, 182, 360] with 11 integration points at 50
²³⁰ μm resolution, yielding a compressed velocity model of ~ 2 GB. This resolution balanced
²³¹ accuracy and computational tractability while remaining portable. All data and code are
²³² publicly available in the accompanying GitHub repository.
²³³ To normalize temporal spacing, we assigned scalar values in $[0, 1]$ to each template. Given the
²³⁴ nonlinear spacing in postnatal development, we applied a logarithmic transform to the raw
²³⁵ time values prior to normalization. P56 was assigned a span of 28 postnatal days to reflect

²³⁶ known developmental dynamics, which improved the temporal distribution of integration
²³⁷ points (Figure 4, right panel).

²³⁸ Optimization was run for a maximum of 200 iterations using a 2020 iMac (3.6 GHz 10-Core
²³⁹ Intel Core i9, 64 GB RAM), with each iteration taking \sim 6 minutes. During each iteration,
²⁴⁰ the velocity field was updated across all 11 integration points by computing regularized
²⁴¹ displacement fields between warped point sets at adjacent time slices. Updates were applied
²⁴² using a step size of $\delta = 0.2$. Convergence was assessed via average displacement error across
²⁴³ all points, with final convergence achieved after \sim 125 iterations (Figure 4, left panel). Median
²⁴⁴ errors across integration points also trended toward zero, albeit at varying rates.

²⁴⁵ **2.2.3 The velocity flow transformation model**

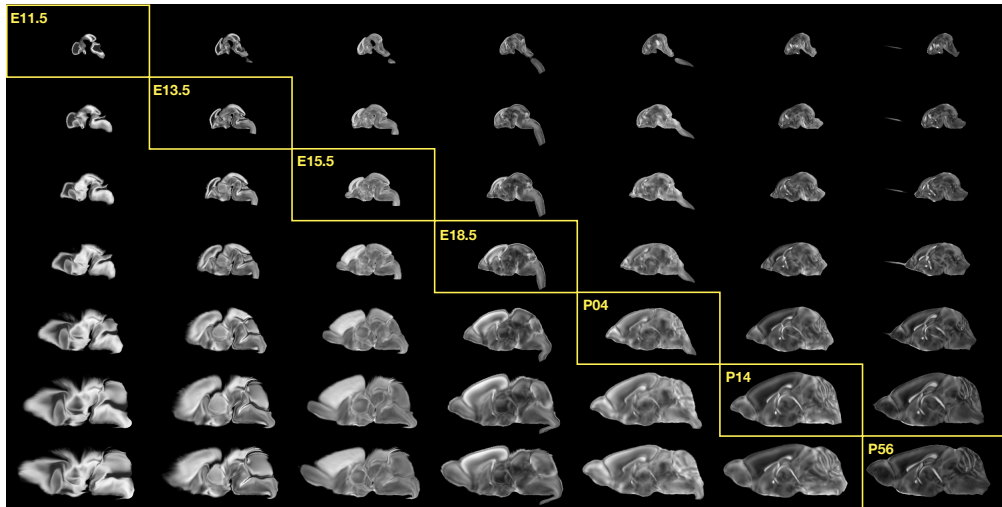


Figure 5: Mid-sagittal visualization of DevCCF templates warped to every other time point. Each row is a reference space; each column is a warped input. Diagonal entries show original templates.

²⁴⁶ Once optimized, the velocity field enables the computation of diffeomorphic transformations
²⁴⁷ between any pair of continuous time points within the DevCCF developmental range. Figure 5
²⁴⁸ illustrates cross-warping between all DevCCF stages using the learned velocity flow model. In
²⁴⁹ addition to facilitating flexible alignment between existing templates, the model also supports
²⁵⁰ the synthesis of virtual templates at intermediate, unsampled developmental stages.

²⁵¹ As shown in Figure 6, we demonstrate the creation of virtual age templates (e.g., P10.3 and

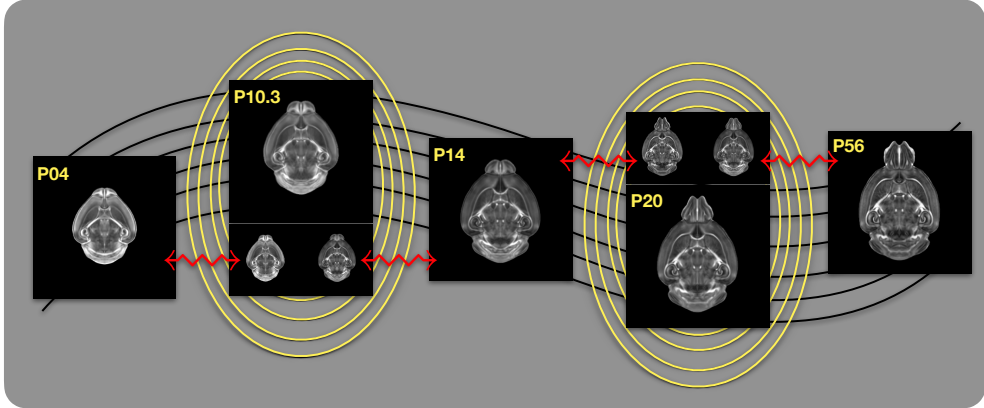


Figure 6: Example of generating “virtual” DevCCF templates at intermediate time points (e.g., P10.3, P20) by warping adjacent stages to a shared time and averaging using ANTsX.

252 P20) by warping adjacent developmental atlases to a target timepoint and constructing an
253 averaged representation using ANTsX’s template-building functionality.

254 All usage examples, scripts, and supporting data are publicly available in the associated
255 codebase.

256 2.3 Automated structural labeling of the mouse brain

257 Structural labeling strategies for the mouse brain are essential for understanding the organi-
258 zation and function of the murine nervous system⁸¹. By dividing the brain into anatomically
259 or functionally defined regions, researchers can localize biological processes, relate regional
260 features to behavior, or quantify spatial variation in gene expression patterns^{82,83}. While deep
261 learning techniques have yielded robust segmentation and labeling tools for the human brain
262 (e.g., SynthSeg⁸⁴, ANTsXNet⁴⁴), analogous development for mouse data has been limited.
263 Mouse neuroimaging often presents unique challenges, such as highly anisotropic sampling,
264 that complicate transfer of existing tools. At the same time, high resolution resources like
265 the AllenCCFv3 and DevCCF provide reference label sets that can serve as training data or
266 spatial priors. We demonstrate how ANTsX can be used to construct a full structural labeling
267 pipeline for the mouse brain (Figure 7), including both brain extraction and atlas-based
268 region segmentation.

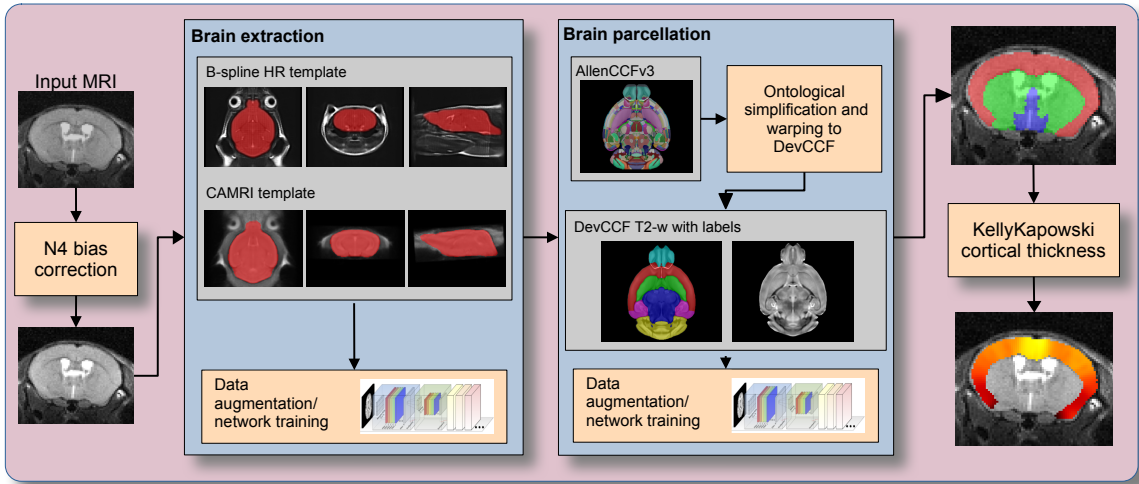


Figure 7: The mouse brain cortical labeling pipeline integrates two deep learning components for brain extraction and anatomical region segmentation. Both networks rely heavily on data augmentation applied to templates constructed from open datasets. The framework also supports further refinement or alternative label sets tailored to specific research needs. Possible applications include voxelwise cortical thickness estimation.

2.3.1 Template-based mouse brain extraction network

To develop a general-purpose mouse brain extraction model, we constructed whole-head templates from two publicly available T2-weighted datasets. The first dataset, from the Center for Animal MRI (CAMRI) at the University of North Carolina at Chapel Hill⁶⁷, includes 16 isotropic MRI volumes acquired at $0.16 \times 0.16 \times 0.16 \text{ mm}^3$ resolution. The second dataset⁶⁸ comprises 88 specimens acquired in three orthogonal 2D views (coronal, axial, sagittal) at $0.08 \times 0.08 \text{ mm}^3$ in-plane resolution with 0.5 mm slice thickness. These orthogonal 2D acquisitions were reconstructed into high-resolution 3D volumes using a B-spline fitting algorithm⁸⁵. Using this synthesized dataset and the CAMRI images, we created two ANTsX-based population templates⁵⁸, each paired with a manually delineated brain mask. These served as the basis for training an initial template-based brain extraction model. Deep learning training of the network employed aggressive data augmentation strategies, including bias field simulation, histogram warping, random spatial deformation, noise injection, and anisotropic resampling. This enabled the model to generalize beyond the two templates. The initial model was released through ANTsXNet and made publicly available.

284 Subsequent community use led to further improvements. A research group applying the
285 tool to their own ex vivo T2-weighted mouse brain data contributed a third template and
286 associated mask (acquired at 0.08 mm isotropic resolution). Incorporating this into the
287 training data improved robustness and accuracy to an independent dataset and extended
288 the model’s generalizability. The refined model is distributed through ANTsPyNet via
289 `antspynet.mouse_brain_extraction(...)`.

290 2.3.2 Template-based mouse brain anatomical labeling

291 The AllenCCFv3 atlas and its hierarchical ontology, along with the DevCCF, provide a strong
292 foundation for developing region-wise anatomical labeling models for multi-modal mouse
293 brain imaging. Using the `allensdk` Python library, we generated a coarse segmentation
294 scheme by grouping anatomical labels into six major regions: cerebral cortex, cerebral nuclei,
295 brainstem, cerebellum, main olfactory bulb, and hippocampal formation. These labels were
296 mapped onto the P56 T2-weighted DevCCF template to serve as training targets. We trained
297 a 3D U-net–based segmentation network using this template and the same augmentation
298 strategies described for brain extraction. The model is publicly available via ANTsXNet
299 (`antspynet.mouse_brain_parcellation(...)`) and supports robust anatomical labeling
300 across diverse imaging geometries and contrasts. The inclusion of aggressive augmentation,
301 including simulated anisotropy, enables the model to perform well even on thick-slice input
302 data. Internally, the model reconstructs isotropic probability and label maps, facilitating
303 downstream morphometric analyses. For example, this network integrates with the ANTsX
304 cortical thickness estimation pipeline (`antspynet.mouse_cortical_thickness(...)`) to
305 produce voxelwise cortical thickness maps, even when applied to anisotropic or limited-
306 resolution mouse brain data.

307 2.3.3 Evaluation

308 For evaluation, we used an additional publicly available dataset⁶⁹ that is completely indepen-
309 dent from the data used in training the brain extraction and parcellation networks. Data
310 includes 12 specimens each imaged at seven time points (Day 0, Day 3, Week 1, Week 4,

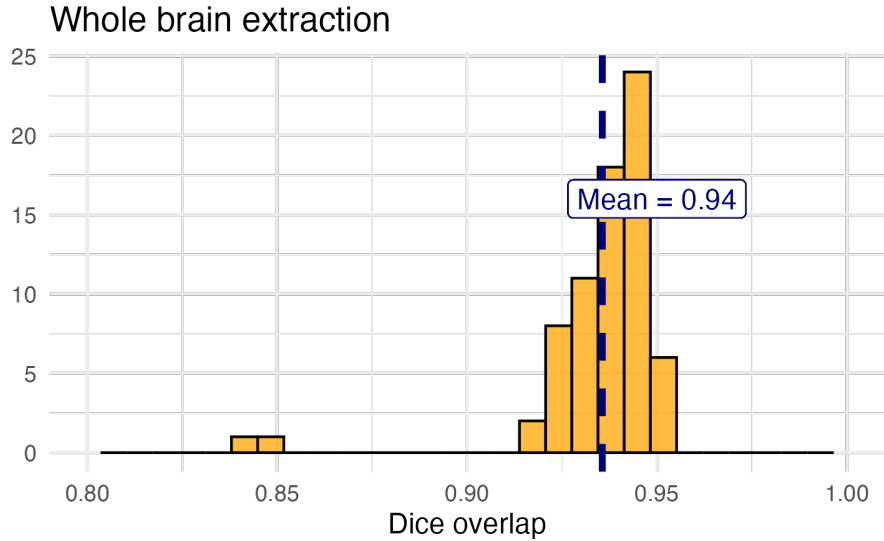
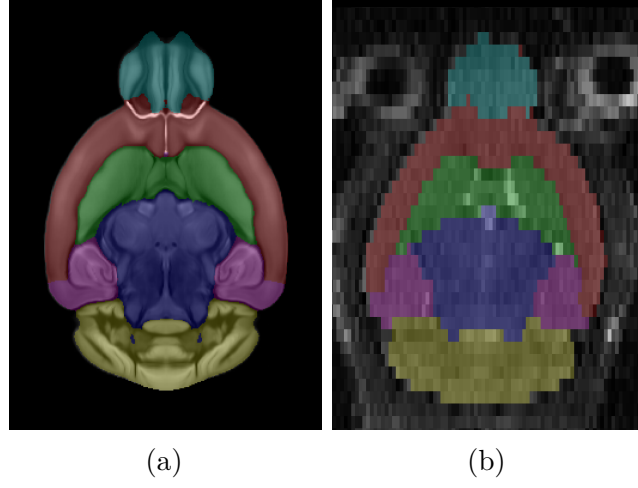


Figure 8: Evaluation of the ANTsX mouse brain extraction on an independent, publicly available dataset consisting of 12 specimens \times 7 time points = 84 total images. Dice overlap comparisons with the user-generated brain masks provide good agreement with the automated results from the brain extraction network.

³¹¹ Week 8, Week 20) with in-house-generated brain masks for a total of 84 images. Spacing is
³¹² anisotropic with an in-plane resolution of $0.1 \times 0.1mm^2$ and a slice thickness of $0.5mm$.

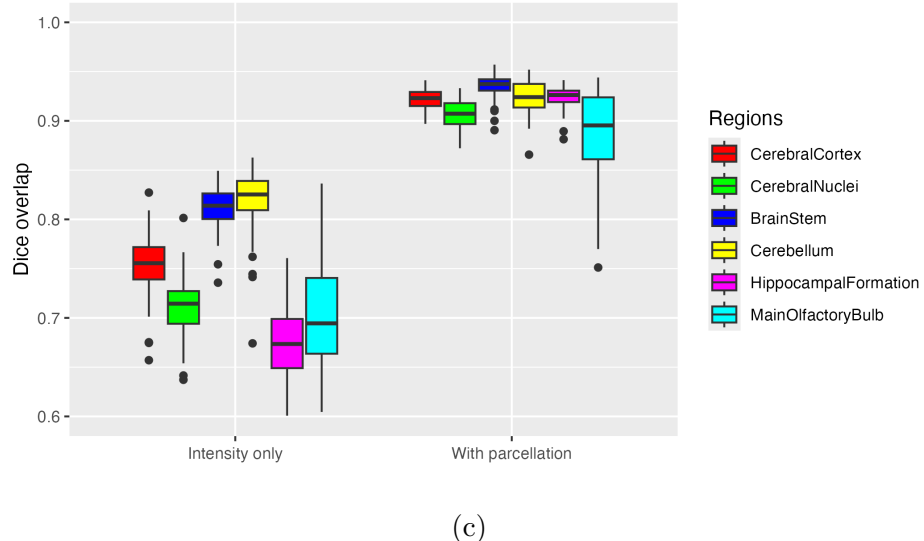
³¹³ Figure 8 summarizes the whole brain overlap between the provided segmentations for all
³¹⁴ 84 images and the results of applying the proposed network. Also, since mapping to the
³¹⁵ AllenCCFv3 atlas is crucial for many mouse studies, we demonstrate the utility of the second
³¹⁶ network by leveraging the labeled regions to perform anatomically-explicit alignment using
³¹⁷ ANTsX multi-component registration instead of intensity-only registration. For these data,
³¹⁸ the whole brain extraction demonstrates excellent performance across the large age range.
³¹⁹ And although the intensity-only image registration provides adequate alignment, intensity
³²⁰ with the regional parcellations significantly improves those measures.



(a)

(b)

Normalization to AllenCCFv3



(c)

Figure 9: Evaluation of the ANTsX mouse brain parcellation on the same dataset. (a) T2-w DevCCF P56 with the described parcellation consisting of the cerebral cortex, nuclei, brain stem, cerebellum, main olfactory bulb, and hippocampal formation. (b) Sample subject (NR5 Day 0) with the proposed deep learning-based segmentation. (c) Dice overlap for comparing the regional alignments between registration using intensity information only and using intensity with the given parcellation scheme.

321 **3 Discussion**

322 The diverse mouse brain cell type profiles gathered through BICCN and associated efforts
323 provide a rich multi-modal resource to the research community. However, despite significant
324 progress, optimal leveraging of these valuable resources remains an ongoing challenge. A
325 central component to data integration is accurately mapping novel cell type data into
326 common coordinate frameworks (CCFs) for subsequent processing and analysis. To meet
327 these needs, tools for mapping mouse brain data must be both broadly accessible and
328 capable of addressing challenges unique to each modality. In this work, we described modular
329 ANTsX-based pipelines developed to support three distinct BICCN efforts encompassing
330 spatial transcriptomic, morphological, and developmental data. We demonstrated how a
331 flexible image analysis toolkit like ANTsX can be tailored to address specific modality-driven
332 constraints by leveraging reusable, validated components.

333 The MERFISH mapping pipeline illustrates how ANTsX tools can be adapted to accommodate
334 high-resolution spatial transcriptomic data. While the general mapping strategy is applicable
335 to other sectioned histological data, the pipeline includes specific adjustments for known
336 anatomical and imaging artifacts present in MERFISH datasets. As such, this example
337 demonstrates how general-purpose tools can be customized to meet the requirements of highly
338 specialized data types.

339 The fMOST mapping pipeline was developed with the intention of broader applicability.
340 Built primarily from existing ANTsX preprocessing and registration modules, this pipeline
341 introduces an fMOST-specific intermediate atlas to facilitate consistent mappings to the
342 AllenCCFv3. The use of a canonical fMOST atlas reduces the need for repeated manual
343 alignment across new datasets, and the resulting transformations can be directly applied to
344 associated single-neuron reconstructions. This supports integrative morphological analysis
345 across specimens using a common coordinate system.

346 For developmental data, we introduced a velocity field-based model for continuous interpo-
347 lation between discrete DevCCF timepoints. Although the DevCCF substantially expands
348 coverage of developmental stages relative to prior atlases, temporal gaps remain. The velocity

349 model enables spatio-temporal transformations within the full developmental interval and
350 supports the generation of virtual templates at unsampled ages. This functionality is built
351 using ANTsX components for velocity field optimization and integration, and offers a novel
352 mechanism for interpolating across the non-linear developmental trajectory of the mouse brain.
353 Such interpolation has potential utility for both anatomical harmonization and longitudinal
354 analyses.

355 We also introduced a template-based deep learning pipeline for mouse brain extraction and
356 parcellation using aggressive data augmentation. This approach is designed to reduce the
357 reliance on large annotated training datasets, which remain limited in the mouse imaging
358 domain. Evaluation on independent data demonstrates promising generalization, though
359 further refinement will be necessary. As with our human-based ANTsX pipelines, failure
360 cases can be manually corrected and recycled into future training cycles. Community
361 contributions are welcomed and encouraged, providing a pathway for continuous improvement
362 and adaptation to new datasets.

363 The ANTsX ecosystem offers a powerful foundation for constructing scalable, reproducible
364 pipelines for mouse brain data analysis. Its modular design and multi-platform support enable
365 researchers to develop customized workflows without extensive new software development.
366 The widespread use of ANTsX components across the neuroimaging community attests to its
367 utility and reliability. As a continuation of the BICCN program, ANTsX is well positioned to
368 support the goals of the BRAIN Initiative Cell Atlas Network (BICAN) and future efforts to
369 extend these mapping strategies to the human brain.

370 **4 Methods**

371 The following methods are all available as part of the ANTsX ecosystem with analogous
372 elements existing in both ANTsR (ANTs in R) and ANTsPy (ANTs in Python), underpinned by
373 a shared ANTs/ITK C++ core. Most development for the work described was performed using
374 ANTsPy. For equivalent functionality in ANTsR, we refer the reader to the comprehensive
375 ANTsX tutorial: <https://tinyurl.com/antsxtutorial>.

376 **4.1 General ANTsX utilities**

377 Although focused on distinct data types, the three pipelines presented in this work share
378 common components that address general challenges in mapping mouse brain data. These
379 include correcting image intensity artifacts, denoising, spatial registration, template generation,
380 and visualization. Table 1 provides a concise summary of the relevant ANTsX functionality.

381 **Preprocessing: bias field correction and denoising.** Standard preprocessing steps in
382 mouse brain imaging include correcting for spatial intensity inhomogeneities and reducing
383 image noise, both of which can impact registration accuracy and downstream analysis. ANTsX
384 provides implementations of widely used methods for these tasks. The N4 bias field correction
385 algorithm⁵¹, originally developed in ANTs and contributed to ITK, mitigates artifactual, low-
386 frequency intensity variation and is accessible via `ants.n4_bias_field_correction(...)`.
387 Patch-based denoising⁶⁰ has been implemented as `ants.denoise_image(...)`.

388 **Image registration.** ANTsX includes a robust and flexible framework for pairwise
389 and groupwise image registration⁸⁶. At its core is the SyN algorithm⁵⁰, a symmetric
390 diffeomorphic model with optional B-spline regularization⁶⁶. In ANTsPy, registration
391 is performed via `ants.registration(...)` using preconfigured parameter sets (e.g.,
392 `antsRegistrationSyNQuick[s]`, `antsRegistrationSyN[s]`) suitable for different imaging
393 modalities and levels of computational demand. Resulting transformations can be applied to
394 new images with `ants.apply_transforms(...)`.

395 **Template generation.** ANTsX supports population-based template generation through
396 iterative pairwise registration to an evolving estimate of the mean shape and intensity

Table 1: Sampling of ANTsX functionality

<i>ANTsPy: Preprocessing</i>	
bias field correction	<code>n4_bias_field_correction(...)</code>
image denoising	<code>denoise_image(...)</code>
<i>ANTsPy: Registration</i>	
image registration	<code>registration(...)</code>
image transformation	<code>apply_transforms(...)</code>
template generation	<code>build_template(...)</code>
landmark registration	<code>fit_transform_to_paired_points(...)</code>
time-varying landmark reg.	<code>fit_time_varying_transform_to_point_sets(...)</code>
integrate velocity field	<code>integrate_velocity_field(...)</code>
invert displacement field	<code>invert_displacement_field(...)</code>
<i>ANTsPy: Segmentation</i>	
MRF-based segmentation	<code>atropos(...)</code>
Joint label fusion	<code>joint_label_fusion(...)</code>
diffeomorphic thickness	<code>kelly_kapowski(...)</code>
<i>ANTsPy: Miscellaneous</i>	
Regional intensity statistics	<code>label_stats(...)</code>
Regional shape measures	<code>label_geometry_measures(...)</code>
B-spline approximation	<code>fit_bspline_object_to_scattered_data(...)</code>
Visualize images and overlays	<code>plot(...)</code>
<i>ANTsPyNet: Mouse-specific</i>	
brain extraction	<code>mouse_brain_extraction(...modality="t2"...)</code>
brain parcellation	<code>mouse_brain_parcellation(...)</code>
cortical thickness	<code>mouse_cortical_thickness(...)</code>
super resolution	<code>mouse_histology_super_resolution(...)</code>

ANTsX provides state-of-the-art functionality for processing biomedical image data. Such tools, including deep learning networks, support a variety of mapping-related tasks. A more comprehensive listing of ANTsX tools with self-contained R and Python examples is provided as a gist page on GitHub (<https://tinyurl.com/antsxtutorial>).

397 reference space across subjects⁵⁸. This functionality was used in generating the DevCCF
398 templates¹⁶. The procedure, implemented as `ants.build_template(...)`, produces average
399 images in both shape and intensity by aligning all inputs to a common evolving template.

400 **Visualization.** To support visual inspection and quality control, ANTsPy provides flexible
401 image visualization with `ants.plot(...)`. This function enables multi-slice and multi-
402 orientation rendering with optional overlays and label maps.

403 4.2 Mapping fMOST data to AllenCCFv3

404 **Preprocessing.** Mapping fMOST data into the AllenCCFv3 presents unique challenges due
405 to its native ultra-high resolution and imaging artifacts common to the fMOST modality.
406 Each fMOST image can exceed a terabyte in size, with spatial resolutions far exceeding
407 those of the AllenCCFv3 ($25\ \mu m$ isotropic). To reduce computational burden and prevent
408 resolution mismatch, each fMOST image is downsampled using cubic B-spline interpolation
409 via `ants.resample_image(...)` to match the template resolution.

410 Stripe artifacts (i.e., periodic intensity distortions caused by nonuniform sectioning or illumina-
411 nation) are common in fMOST and can mislead deformable registration algorithms. These
412 were removed using a custom 3D notch filter (`remove_stripe_artifact(...)`) implemented
413 in the `CCFAlignmentToolkit` using SciPy frequency domain filtering. The filter targets
414 dominant stripe frequencies along a user-specified axis in the Fourier domain. In addition,
415 intensity inhomogeneity across sections, often arising from variable staining or illumination,
416 was corrected using N4 bias field correction.

417 **Template-based spatial normalization.** To facilitate reproducible mapping, we first
418 constructed a contralaterally symmetric average template from 30 fMOST brains and their
419 mirrored counterparts using ANTsX template-building tools. Because the AllenCCFv3 and
420 fMOST data differ substantially in both intensity contrast and morphology, direct deformable
421 registration between individual fMOST brains and the AllenCCFv3 was insufficiently robust.
422 Instead, we performed a one-time expert-guided label-driven registration between the average
423 fMOST template and AllenCCFv3. This involved sequential alignment of seven manually

424 selected anatomical regions: 1) brain mask/ventricles, 2) caudate/putamen, 3) fimbria, 4)
425 posterior choroid plexus, 5) optic chiasm, 6) anterior choroid plexus, and 7) habenular
426 commissure which were prioritized to enable coarse-to-fine correction of shape differences.
427 Once established, this fMOST-template-to-AllenCCFv3 transform was reused for all subse-
428 quent specimens. Each new fMOST brain was then registered to the average fMOST template
429 using intensity-based registration, followed by concatenation of transforms to produce the
430 final mapping into AllenCCFv3 space.

431 **Mapping neuron projections.** A key advantage of fMOST imaging is its ability to
432 support single neuron projection reconstruction across the entire brain⁷⁷. Because these
433 reconstructions are stored as 3D point sets aligned to the original fMOST volume, we applied
434 the same composite transform used for image alignment to the point data using ANTsX
435 functionality. This enables seamless integration of cellular morphology data into AllenCCFv3
436 space, facilitating comparative analyses across specimens.

437 4.3 Mapping MERFISH data to AllenCCFv3

438 **Preprocessing.** MERFISH data are acquired as a series of 2D tissue sections, each comprising
439 spatially localized gene expression measurements at subcellular resolution. To enable 3D
440 mapping to the AllenCCFv3, we first constructed anatomical reference images by aggregating
441 the number of detected transcripts per voxel across all probes within each section. These 2D
442 projections were resampled to a resolution of $10 \mu m \times 10 \mu m$ to match the in-plane resolution
443 of the AllenCCFv3.

444 Sections were coarsely aligned using manually annotated dorsal and ventral midline points,
445 allowing initial volumetric reconstruction. However, anatomical fidelity remained limited by
446 variation in section orientation, spacing, and tissue loss. To further constrain alignment and
447 enable deformable registration, we derived region-level anatomical labels directly from the
448 gene expression data.

449 **Label creation.** We assigned each detected cell to one of 15 coarse anatomical regions (e.g.,
450 hippocampus, cortex, striatum—using transcriptomic similarity to scRNA) seq reference

451 data. These assignments were aggregated across spatial grids to produce probabilistic label
452 maps for each section. To ensure full regional coverage, morphological dilation was applied to
453 fill gaps between sparsely distributed cells. Finer-resolution structures (e.g., cortical layers,
454 habenula) were similarly labeled using marker gene enrichment and spatial constraints. This
455 dual-level labeling (i.e., coarse and fine) allowed us to construct a robust anatomical scaffold
456 in the MERFISH coordinate system that could be matched to AllenCCFv3 annotations.

457 **Section matching via global alignment.** A major challenge was compensating for oblique
458 cutting angles and non-uniform section thickness, which distort the anatomical shape and
459 spacing of the reconstructed volume. Rather than directly warping the MERFISH data into
460 atlas space, we globally aligned the AllenCCFv3 to the MERFISH coordinate system. This
461 was done via an affine transformation followed by resampling of AllenCCFv3 sections to match
462 the number and orientation of MERFISH sections. This approach minimizes interpolation
463 artifacts in the MERFISH data and facilitates one-to-one section matching.

464 **Landmark-driven deformable alignment.** We used a 2.5D approach for fine alignment of
465 individual sections. In each MERFISH slice, deformable registration was driven by sequential
466 alignment of anatomical landmarks between the label maps derived from MERFISH and
467 AllenCCFv3. A total of nine regions—including isocortical layers 2/3, 5, and 6, the striatum,
468 hippocampus, thalamus, and medial/lateral habenula—were registered in an empirically
469 determined order. After each round, anatomical alignment was visually assessed by an expert,
470 and the next structure was selected to maximize improvement in the remaining misaligned
471 regions.

472 The final transform for each section combined the global affine alignment and the per-structure
473 deformable registrations. These were concatenated to generate a 3D mapping from the original
474 MERFISH space to the AllenCCFv3 coordinate system. Once established, the composite
475 mapping enables direct transfer of gene-level and cell-type data from MERFISH into atlas
476 space, allowing integration with other imaging and annotation datasets.

477 **4.4 DevCCF velocity flow transformation model**

478 The Developmental Common Coordinate Framework (DevCCF)¹⁶ provides a discrete set of
479 age-specific templates that temporally sample the developmental trajectory. To model this
480 biological progression more continuously, we introduce a velocity flow-based paradigm for
481 inferring diffeomorphic transformations between developmental stages. This enables anatom-
482 ically plausible estimation of intermediate templates or mappings at arbitrary timepoints
483 between the E11.5 and P56 endpoints of the DevCCF. Our approach builds on established
484 insights from time-varying diffeomorphic registration⁶⁵, where a velocity field governs the
485 smooth deformation of anatomical structures over time. Importantly, the framework is
486 extensible and can naturally accommodate additional timepoints for the potential expansion
487 of the DevCCF.

488 **Point sampling and region correspondence.** We first coalesced the anatomical labels
489 across the seven DevCCF templates (E11.5, E13.5, E15.5, E18.5, P4, P14, P56) into 26
490 common structures that could be consistently identified across development. These include
491 major brain regions such as the cortex, cerebellum, hippocampus, midbrain, and ventricles.
492 For each successive pair of templates, we performed multi-label deformable registration
493 using ANTsX to generate forward and inverse transforms between anatomical label volumes.
494 From the P56 space, we randomly sampled approximately 1e6 points within and along the
495 boundaries of each labeled region and propagated them through each pairwise mapping step
496 (e.g., P56 → P14, P14 → P4, ..., E13.5 → E11.5). This procedure created time-indexed
497 point sets tracing the spatial evolution of each region.

498 **Velocity field fitting.** Using these point sets, we fit a continuous velocity field over
499 developmental time using a generalized B-spline scattered data approximation method⁸⁵.
500 The field was parameterized over a log-scaled time axis to ensure finer temporal resolution
501 during early embryonic stages, where morphological changes are most rapid. Optimization
502 proceeded for approximately 125 iterations, minimizing the average Euclidean norm between
503 transformed points at each step. Ten integration points were used to ensure numerical
504 stability. The result is a smooth, differentiable vector field that defines a diffeomorphic
505 transform between any two timepoints within the template range.

506 **Applications and availability.** This velocity model can be used to estimate spatial transfor-
507 mations between any pair of developmental stages—even those for which no empirical template
508 exists—allowing researchers to create interpolated atlases, align new datasets, or measure con-
509 tinuous structural changes. It also enables developmental alignment of multi-modal data (e.g.,
510 MRI to LSFM) by acting as a unifying spatiotemporal scaffold. The underlying components
511 for velocity field fitting and integration are implemented in ITK, and the complete workflow
512 is accessible in both ANTsPy (`ants.fit_time_varying_transform_to_point_sets(...)`)
513 and ANTsR. In addition the availability of the DevCCF use case, self-contained examples
514 and usage tutorials are provided in our public codebase.

515 4.5 Automated brain extraction and parcellation with ANTsXNet

516 To support template-based deep learning approaches for structural brain extraction and par-
517 cellation, we implemented dedicated pipelines using the ANTsXNet framework. ANTsXNet
518 comprises open-source deep learning libraries in both Python (ANTsPyNet) and R (ANTsR-
519 Net) that interface with the broader ANTsX ecosystem and are built on TensorFlow/Keras.
520 Our mouse brain pipelines mirror existing ANTsXNet tools for human imaging but are
521 adapted for species-specific anatomical variation, lower SNR, and heterogeneous acquisition
522 protocols.

523 4.5.1 Deep learning training setup

524 All networks were implemented in ANTsPyNet using standard 3D U-net architectures⁸⁷
525 previously employed in previously published work⁴⁴. Training was performed on an NVIDIA
526 DGX system (4 × Tesla V100 GPUs, 256 GB RAM). Model weights and preprocessing
527 routines are shared across ANTsPyNet and ANTsRNet to ensure reproducibility and lan-
528 guage portability. For both published and unpublished trained networks available through
529 ANTsXNet, all training scripts and data augmentation generators are publicly available at
530 <https://github.com/ntustison/ANTsXNetTraining>.

531 **Data augmentation.** Robust data augmentation was critical to generalization across

532 scanners, contrast types, and resolutions. We applied both intensity- and shape-based
533 augmentation strategies:

534 • *Intensity augmentations:*

- 535 – Gaussian, Poisson, and salt-and-pepper noise:
536 `ants.add_noise_to_image(...)`
- 537 – Simulated intensity inhomogeneity via bias field modeling⁵¹:
538 `antspynet.simulate_bias_field(...)`
- 539 – Histogram warping to simulate contrast variation⁸⁸:
540 `antspynet.histogram_warp_image_intensities(...)`

541 • *Shape augmentations:*

- 542 – Random nonlinear deformations and affine transforms:
543 `antspynet.randomly_transform_image_data(...)`
- 544 – Anisotropic resampling across axial, sagittal, and coronal planes:
545 `ants.resample_image(...)`

546 **4.5.2 Brain extraction**

547 We originally trained a mouse-specific brain extraction model on two manually masked
548 T2-weighted templates, generated from public datasets^{67,68}. One of the templates was
549 constructed from orthogonal 2D acquisitions using B-spline-based volumetric synthesis
550 via `ants.fit_bspline_object_to_scattered_data(...)`. Normalized gradient magnitude
551 was used as a weighting function to emphasize boundaries during reconstruction⁸⁵.

552 This training strategy provides strong spatial priors despite limited data by leveraging
553 high-quality template images and aggressive augmentation to mimic population variability.
554 During the development of this work, the network was further refined through community
555 engagement. A user from a U.S.-based research institute applied the publicly available (but
556 then unpublished) brain extraction tool to their own mouse MRI dataset. Based on feedback
557 and iterative collaboration with the ANTsX team, the model was retrained and improved to

558 better generalize to additional imaging contexts. This reflects our broader commitment to
559 community-driven development and responsiveness to user needs across diverse mouse brain
560 imaging scenarios.

561 The final trained network is available via ANTsXNet through the function
562 `antspynet.mouse_brain_extraction(...)`. Additionally, both template/mask pairs are
563 accessible via ANTsXNet. For example, one such image pair is available via:

- 564 • Template:

565 `antspynet.get_antsxnet_data("bsplineT2MouseTemplate")`

- 566 • Brain mask:

567 `antspynet.get_antsxnet_data("bsplineT2MouseTemplateBrainMask")`

568 4.5.3 Brain parcellation

569 For brain parcellation, we trained a 3D U-net model using the DevCCF P56 T2-weighted
570 template and anatomical segmentations derived from AllenCCFv3. This template-based
571 training strategy enables the model to produce accurate, multi-region parcellations without
572 requiring large-scale annotated subject data.

573 To normalize intensity across specimens, input images were preprocessed using rank-based
574 intensity normalization (`ants.rank_intensity(...)`). Spatial harmonization was achieved
575 through affine and deformable alignment of each extracted brain to the P56 template prior
576 to inference. In addition to the normalized image input, the network also receives prior
577 probability maps derived from the atlas segmentations, providing additional spatial context.

578 This general parcellation deep learning framework has also been applied in collaboration
579 with other groups pursuing related but distinct projects. In one case, a model variant
580 was adapted for T2-weighted MRI using an alternative anatomical labeling scheme; in
581 another, a separate model was developed for serial two-photon tomography (STPT) with
582 a different parcellation set. All three models are accessible through a shared interface
583 in ANTsXNet: `antspynet.mouse_brain_parcellation(...)`. Ongoing work is further
584 extending this approach to embryonic mouse brain data. These independent efforts reflect

585 broader community interest in adaptable parcellation tools and reinforce the utility of
586 ANTsXNet as a platform for reproducible, extensible deep learning workflows.

587 **4.5.4 Evaluation and reuse**

588 To assess model generalizability, both the brain extraction and parcellation networks were
589 evaluated on an independent longitudinal dataset comprising multiple imaging sessions
590 with varied acquisition parameters⁶⁹. Although each label or imaging modality required
591 retraining, the process was streamlined by the reusable ANTsX infrastructure enabled by
592 rapid adaptation with minimal overhead. These results illustrate the practical benefits of a
593 template-based, low-shot strategy and modular deep learning framework. All trained models,
594 associated training scripts, and supporting resources are openly available and designed for
595 straightforward integration into ANTsX workflows.

596 **Data availability**

597 All data and software used in this work are publicly available. The DevCCF atlas is
598 available at <https://kimlab.io/brain-map/DevCCF/>. ANTsPy, ANTsR, ANTsPyNet, and
599 ANTsRNet are available through GitHub at the ANTsX Ecosystem (<https://github.com/ANTsX>). Training scripts for all deep learning functionality in ANTsXNet can also be found on
600 GitHub (<https://github.com/ntustison/ANTsXNetTraining>). A GitHub repository specifically
601 pertaining to the AllenCCFv3 mapping is available at <https://github.com/dontminchenit/>
602 [CCFAAlignmentToolkit](#). For the other two contributions contained in this work, the longitudinal
603 DevCCF mapping and mouse cortical thickness pipeline, we refer the interested reader to
604 <https://github.com/ntustison/ANTsXMouseBrainMapping>.

606 **Acknowledgments**

607 Support for the research reported in this work includes funding from the National Institute
608 of Biomedical Imaging and Bioengineering (R01-EB031722) and National Institute of Mental
609 Health (RF1-MH124605 and U24-MH114827).

610 We also acknowledge the data contribution of Dr. Adam Raikes (GitHub @araikes) of the
611 Center for Innovation in Brain Science at the University of Arizona for refining the weights
612 of the mouse brain extraction network.

⁶¹³ **Author contributions**

⁶¹⁴ N.T., M.C., and J.G. wrote the main manuscript text and figures. M.C., M.K., R.D., S.S.,
⁶¹⁵ Q.W., L.G., J.D., C.G., and J.G. developed the Allen registration pipelines. N.T. and F.K.
⁶¹⁶ developed the time-varying velocity transformation model for the DevCCF. N.T. and M.T.
⁶¹⁷ developed the brain parcellation and cortical thickness methodology. All authors reviewed
⁶¹⁸ the manuscript.

619 **References**

- 620 1. Keller, P. J. & Ahrens, M. B. Visualizing whole-brain activity and development at the single-cell level using light-sheet microscopy. *Neuron* **85**, 462–83 (2015).
- 621 2. La Manno, G. *et al.* Molecular architecture of the developing mouse brain. *Nature* **596**, 92–96 (2021).
- 622 3. Wen, L. *et al.* Single-cell technologies: From research to application. *Innovation (Camb)* **3**, 100342 (2022).
- 623 4. Oh, S. W. *et al.* A mesoscale connectome of the mouse brain. *Nature* **508**, 207–14 (2014).
- 624 5. Gong, H. *et al.* Continuously tracing brain-wide long-distance axonal projections in mice at a one-micron voxel resolution. *Neuroimage* **74**, 87–98 (2013).
- 625 6. Li, A. *et al.* Micro-optical sectioning tomography to obtain a high-resolution atlas of the mouse brain. *Science* **330**, 1404–8 (2010).
- 626 7. Ueda, H. R. *et al.* Tissue clearing and its applications in neuroscience. *Nat Rev Neurosci* **21**, 61–79 (2020).
- 627 8. Ståhl, P. L. *et al.* Visualization and analysis of gene expression in tissue sections by spatial transcriptomics. *Science* **353**, 78–82 (2016).
- 628 9. Burgess, D. J. Spatial transcriptomics coming of age. *Nat Rev Genet* **20**, 317 (2019).
- 629 10. Hardwick, S. A. *et al.* Single-nuclei isoform RNA sequencing unlocks barcoded exon connectivity in frozen brain tissue. *Nature biotechnology* **40**, 1082–1092 (2022).
- 630 11. Hawrylycz, M. *et al.* A guide to the BRAIN initiative cell census network data ecosystem. *PLoS biology* **21**, e3002133 (2023).
- 631 12. Wang, Q. *et al.* The allen mouse brain common coordinate framework: A 3D reference atlas. *Cell* **181**, 936–953.e20 (2020).
- 632 13. Perens, J. *et al.* An optimized mouse brain atlas for automated mapping and quantification of neuronal activity using iDISCO+ and light sheet fluorescence microscopy. *Neuroinformatics* **19**, 433–446 (2021).
- 633 14. Ma, Y. *et al.* A three-dimensional digital atlas database of the adult C57BL/6J mouse brain by magnetic resonance microscopy. *Neuroscience* **135**, 1203–1215 (2005).

- 634 15. Qu, L. *et al.* Cross-modal coherent registration of whole mouse brains. *Nature Methods* **19**, 111–118 (2022).
- 635 16. Kronman, F. N. *et al.* [Developmental mouse brain common coordinate framework](#). *Nat Commun* **15**, 9072 (2024).
- 636 17. Chuang, N. *et al.* An MRI-based atlas and database of the developing mouse brain. *Neuroimage* **54**, 80–89 (2011).
- 637 18. Dries, R. *et al.* Advances in spatial transcriptomic data analysis. *Genome research* **31**, 1706–1718 (2021).
- 638 19. Ricci, P. *et al.* Removing striping artifacts in light-sheet fluorescence microscopy: A review. *Progress in biophysics and molecular biology* **168**, 52–65 (2022).
- 639 20. Agarwal, N., Xu, X. & Gopi, M. Robust registration of mouse brain slices with severe histological artifacts. in *Proceedings of the tenth indian conference on computer vision, graphics and image processing* 1–8 (2016).
- 640 21. Agarwal, N., Xu, X. & Gopi, M. Automatic detection of histological artifacts in mouse brain slice images. in *Medical computer vision and bayesian and graphical models for biomedical imaging: MICCAI 2016 international workshops, MCV and BAMBI, athens, greece, october 21, 2016, revised selected papers* 8 105–115 (Springer, 2017).
- 641 22. Tward, D. *et al.* 3d mapping of serial histology sections with anomalies using a novel robust deformable registration algorithm. in *International workshop on multimodal brain image analysis* 162–173 (Springer, 2019).
- 642 23. Cahill, L. S. *et al.* Preparation of fixed mouse brains for MRI. *Neuroimage* **60**, 933–939 (2012).
- 643 24. Sunkin, S. M. *et al.* Allen brain atlas: An integrated spatio-temporal portal for exploring the central nervous system. *Nucleic acids research* **41**, D996–D1008 (2012).
- 644 25. Kim, Y. *et al.* Brain-wide maps reveal stereotyped cell-type-based cortical architecture and subcortical sexual dimorphism. *Cell* **171**, 456–469 (2017).
- 645 26. Fürth, D. *et al.* [An interactive framework for whole-brain maps at cellular resolution](#). *Nat Neurosci* **21**, 139–149 (2018).

- 646 27. Li, Y. *et al.* mBrainAligner-web: A web server for cross-modal coherent registration
of whole mouse brains. *Bioinformatics* **38**, 4654–4655 (2022).
- 647 28. Puchades, M. A., Csucs, G., Ledergerber, D., Leergaard, T. B. & Bjaalie, J. G. Spatial
registration of serial microscopic brain images to three-dimensional reference atlases
with the QuickNII tool. *PloS one* **14**, e0216796 (2019).
- 648 29. Eastwood, B. S. *et al.* Whole mouse brain reconstruction and registration to a
reference atlas with standard histochemical processing of coronal sections. *Journal of
Comparative Neurology* **527**, 2170–2178 (2019).
- 649 30. Ni, H. *et al.* A robust image registration interface for large volume brain atlas. *Sci
Rep* **10**, 2139 (2020).
- 650 31. Pallast, N. *et al.* Processing pipeline for atlas-based imaging data analysis of structural
and functional mouse brain MRI (AIDAmri). *Front Neuroinform* **13**, 42 (2019).
- 651 32. Celestine, M., Nadkarni, N. A., Garin, C. M., Bougacha, S. & Dhenain, M. **Sammba-
MRI: A library for processing SmAll-MaMmal BrAin MRI data in python**. *Front
Neuroinform* **14**, 24 (2020).
- 652 33. Ioanas, H.-I., Marks, M., Zerbi, V., Yanik, M. F. & Rudin, M. An optimized registration
workflow and standard geometric space for small animal brain imaging. *Neuroimage*
241, 118386 (2021).
- 653 34. Aggarwal, M., Zhang, J., Miller, M. I., Sidman, R. L. & Mori, S. Magnetic resonance
imaging and micro-computed tomography combined atlas of developing and adult
mouse brains for stereotaxic surgery. *Neuroscience* **162**, 1339–1350 (2009).
- 654 35. Chandrashekhar, V. *et al.* CloudReg: Automatic terabyte-scale cross-modal brain
volume registration. *Nature methods* **18**, 845–846 (2021).
- 655 36. Jin, M. *et al.* SMART: An open-source extension of WholeBrain for intact mouse
brain registration and segmentation. *eNeuro* **9**, (2022).
- 656 37. Negwer, M. *et al.* FriendlyClearMap: An optimized toolkit for mouse brain mapping
and analysis. *Gigascience* **12**, (2022).
- 657 38. Lin, W. *et al.* Whole-brain mapping of histaminergic projections in mouse brain.
Proceedings of the National Academy of Sciences **120**, e2216231120 (2023).

- 658 39. Zhang, M. *et al.* Spatially resolved cell atlas of the mouse primary motor cortex by MERFISH. *Nature* **598**, 137–143 (2021).
- 659 40. Shi, H. *et al.* Spatial atlas of the mouse central nervous system at molecular resolution. *Nature* **622**, 552–561 (2023).
- 660 41. Zhang, Y. *et al.* Reference-based cell type matching of *in situ* image-based spatial transcriptomics data on primary visual cortex of mouse brain. *Scientific Reports* **13**, 9567 (2023).
- 661 42. Klein, S., Staring, M., Murphy, K., Viergever, M. A. & Pluim, J. P. W. [Elastix: A toolbox for intensity-based medical image registration](#). *IEEE Trans Med Imaging* **29**, 196–205 (2010).
- 662 43. Fedorov, A. *et al.* 3D slicer as an image computing platform for the quantitative imaging network. *Magnetic resonance imaging* **30**, 1323–1341 (2012).
- 663 44. Tustison, N. J. *et al.* [The ANTsX ecosystem for quantitative biological and medical imaging](#). *Sci Rep* **11**, 9068 (2021).
- 664 45. Rolfe, S. M., Whikehart, S. M. & Maga, A. M. [Deep learning enabled multi-organ segmentation of mouse embryos](#). *Biol Open* **12**, bio059698 (2023).
- 665 46. Pagani, M., Damiano, M., Galbusera, A., Tsafaris, S. A. & Gozzi, A. Semi-automated registration-based anatomical labelling, voxel based morphometry and cortical thickness mapping of the mouse brain. *Journal of neuroscience methods* **267**, 62–73 (2016).
- 666 47. Anderson, R. J. *et al.* [Small animal multivariate brain analysis \(SAMBA\) - a high throughput pipeline with a validation framework](#). *Neuroinformatics* **17**, 451–472 (2019).
- 667 48. Allan Johnson, G. *et al.* Whole mouse brain connectomics. *Journal of Comparative Neurology* **527**, 2146–2157 (2019).
- 668 49. Yao, Z. *et al.* [A high-resolution transcriptomic and spatial atlas of cell types in the whole mouse brain](#). *Nature* **624**, 317–332 (2023).

- 669 50. Avants, B. B., Epstein, C. L., Grossman, M. & Gee, J. C. [Symmetric diffeomorphic](#)
image registration with cross-correlation: Evaluating automated labeling of elderly
and neurodegenerative brain. *Med Image Anal* **12**, 26–41 (2008).
- 670 51. Tustison, N. J. *et al.* [N4ITK: Improved N3 bias correction](#). *IEEE Trans Med Imaging*
29, 1310–20 (2010).
- 671 52. Bajcsy, R. & Broit, C. Matching of deformed images. in *Sixth International Conference*
on Pattern Recognition (ICPR'82) 351–353 (1982).
- 672 53. Bajcsy, R. & Kovacic, S. [Multiresolution elastic matching](#). *Computer Vision, Graphics,*
and Image Processing **46**, 1–21 (1989).
- 673 54. Gee, J. C., Reivich, M. & Bajcsy, R. [Elastically deforming 3D atlas to match anatomical](#)
[brain images](#). *J Comput Assist Tomogr* **17**, 225–36 (1993).
- 674 55. Klein, A. *et al.* [Evaluation of 14 nonlinear deformation algorithms applied to human](#)
[brain MRI registration](#). *Neuroimage* **46**, 786–802 (2009).
- 675 56. Murphy, K. *et al.* [Evaluation of registration methods on thoracic CT: The EMPIRE10](#)
[challenge](#). *IEEE Trans Med Imaging* **30**, 1901–20 (2011).
- 676 57. Baheti, B. *et al.* [The brain tumor sequence registration challenge: Establishing](#)
correspondence between pre-operative and follow-up MRI scans of diffuse glioma
patients. (2021).
- 677 58. Avants, B. B. *et al.* [The optimal template effect in hippocampus studies of diseased](#)
[populations](#). *Neuroimage* **49**, 2457–66 (2010).
- 678 59. Avants, B. B., Tustison, N. J., Wu, J., Cook, P. A. & Gee, J. C. [An open source](#)
[multivariate framework for n-tissue segmentation with evaluation on public data](#).
Neuroinformatics **9**, 381–400 (2011).
- 679 60. Manjón, J. V., Coupé, P., Martí-Bonmatí, L., Collins, D. L. & Robles, M. [Adaptive](#)
[non-local means denoising of MR images with spatially varying noise levels](#). *J Magn*
Reson Imaging **31**, 192–203 (2010).
- 680 61. Wang, H. *et al.* [Multi-atlas segmentation with joint label fusion](#). *IEEE Trans Pattern*
Anal Mach Intell **35**, 611–23 (2013).

- 681 62. Tustison, N. J. *et al.* Optimal symmetric multimodal templates and concatenated
random forests for supervised brain tumor segmentation (simplified) with *ANTsR*.
Neuroinformatics (2014) doi:10.1007/s12021-014-9245-2.
- 682 63. Tustison, N. J., Yang, Y. & Salerno, M. Advanced normalization tools for cardiac
motion correction. in *Statistical atlases and computational models of the heart -*
imaging and modelling challenges (eds. Camara, O. et al.) vol. 8896 3–12 (Springer
International Publishing, 2015).
- 683 64. McCormick, M., Liu, X., Jomier, J., Marion, C. & Ibanez, L. ITK: Enabling repro-
ducible research and open science. *Front Neuroinform* **8**, 13 (2014).
- 684 65. Beg, M. F., Miller, M. I., Trouvé, A. & Younes, L. Computing large deformation metric
mappings via geodesic flows of diffeomorphisms. *International Journal of Computer
Vision* **61**, 139–157 (2005).
- 685 66. Tustison, N. J. & Avants, B. B. Explicit B-spline regularization in diffeomorphic image
registration. *Front Neuroinform* **7**, 39 (2013).
- 686 67. Hsu, L.-M. *et al.* CAMRI mouse brain MRI data.
- 687 68. Reshetnikov, V. *et al.* High-resolution MRI data of brain C57BL/6 and BTBR mice
in three different anatomical views.
- 688 69. Rahman, N., Xu, K., Budde, M. D., Brown, A. & Baron, C. A. A longitudinal
microstructural MRI dataset in healthy C57Bl/6 mice at 9.4 tesla. *Sci Data* **10**, 94
(2023).
- 689 70. Liu, J. *et al.* Concordance of MERFISH spatial transcriptomics with bulk and
single-cell RNA sequencing. *Life Sci Alliance* **6**, (2023).
- 690 71. Stringer, C., Wang, T., Michaelos, M. & Pachitariu, M. Cellpose: A generalist
algorithm for cellular segmentation. *Nat Methods* **18**, 100–106 (2021).
- 691 72. Jia, H., Yap, P.-T., Wu, G., Wang, Q. & Shen, D. Intermediate templates guided
groupwise registration of diffusion tensor images. *NeuroImage* **54**, 928–939 (2011).
- 692 73. Tang, S., Fan, Y., Wu, G., Kim, M. & Shen, D. RABBIT: Rapid alignment of brains
by building intermediate templates. *NeuroImage* **47**, 1277–1287 (2009).

- 693 74. Dewey, B. E., Carass, A., Blitz, A. M. & Prince, J. L. Efficient multi-atlas registration
using an intermediate template image. in *Proceedings of SPIE—the international society
for optical engineering* vol. 10137 (NIH Public Access, 2017).
- 694 75. Perens, J. *et al.* Multimodal 3D mouse brain atlas framework with the skull-derived
coordinate system. *Neuroinformatics* **21**, 269–286 (2023).
- 695 76. Rotolo, T., Smallwood, P. M., Williams, J. & Nathans, J. Genetically-directed, cell
type-specific sparse labeling for the analysis of neuronal morphology. *PLoS One* **3**,
e4099 (2008).
- 696 77. Peng, H. *et al.* Morphological diversity of single neurons in molecularly defined cell
types. *Nature* **598**, 174–181 (2021).
- 697 78. Gong, H. *et al.* High-throughput dual-colour precision imaging for brain-wide connec-
tome with cytoarchitectonic landmarks at the cellular level. *Nat Commun* **7**, 12142
(2016).
- 698 79. Wang, J. *et al.* Divergent projection patterns revealed by reconstruction of individual
neurons in orbitofrontal cortex. *Neurosci Bull* **37**, 461–477 (2021).
- 699 80. Kronman, F. A. *et al.* Developmental mouse brain common coordinate framework.
bioRxiv (2023) doi:[10.1101/2023.09.14.557789](https://doi.org/10.1101/2023.09.14.557789).
- 700 81. Chon, U., Vanselow, D. J., Cheng, K. C. & Kim, Y. Enhanced and unified anatomical
labeling for a common mouse brain atlas. *Nat Commun* **10**, 5067 (2019).
- 701 82. Tasic, B. *et al.* Adult mouse cortical cell taxonomy revealed by single cell transcript-
omics. *Nat Neurosci* **19**, 335–46 (2016).
- 702 83. Bergmann, E., Gofman, X., Kavushansky, A. & Kahn, I. Individual variability in
functional connectivity architecture of the mouse brain. *Commun Biol* **3**, 738 (2020).
- 703 84. Billot, B. *et al.* SynthSeg: Segmentation of brain MRI scans of any contrast and
resolution without retraining. *Med Image Anal* **86**, 102789 (2023).
- 704 85. Tustison, N. J. & Amini, A. A. Biventricular myocardial strains via nonrigid registration
of anatomical NURBS model [corrected]. *IEEE Trans Med Imaging* **25**, 94–112 (2006).
- 705 86. Avants, B. B. *et al.* The Insight ToolKit image registration framework. *Front Neu-
roinform* **8**, 44 (2014).

- 706 87. Falk, T. *et al.* U-net: Deep learning for cell counting, detection, and morphometry. *Nat Methods* **16**, 67–70 (2019).
- 707 88. Tustison, N. J. *et al.* Image- versus histogram-based considerations in semantic segmentation of pulmonary hyperpolarized gas images. *Magn Reson Med* **86**, 2822–2836 (2021).